Optical methodology for detecting histologically unapparent nanoscale consequences of genetic alterations in biological cells

Hariharan Subramanian[a,1], Prabhakar Pradhan[a], Yang Liu[a], Ilker R. Capoglu[a], Xu Li[a,b], Jeremy D. Rogers[a], Alexander Heifetz[a], Dhananjay Kunte[c], Hemant K. Roy[c], Allen Taflove[b], and Vadim Backman[a,1]

Departments of [a]Biomedical Engineering and [b]Electrical Engineering and Computer Science, Northwestern University, Evanston, IL 60208; and [c]Department of Internal Medicine, Evanston Northwestern Healthcare, Evanston, IL 60208

Edited by Shu Chien, University of California at San Diego, La Jolla, CA, and approved October 16, 2008 (received for review May 17, 2008)

Recently, there has been a major thrust to understand biological processes at the nanoscale. Optical microscopy has been exceedingly useful in imaging cell microarchitecture. Characterization of cell organization at the nanoscale, however, has been stymied by the lack of practical means of cell analysis at these small scales. To address this need, we developed a microscopic spectroscopy technique, single-cell partial-wave spectroscopy (PWS), which provides insights into the statistical properties of the nanoscale architecture of biological cells beyond what conventional microscopy reveals. Coupled with the mesoscopic light transport theory, PWS quantifies the disorder strength of intracellular architecture. As an illustration of the potential of the technique, in the experiments with cell lines and an animal model of colon carcinogenesis we show that increase in the degree of disorder in cell nanoarchitecture parallels genetic events in the early stages of carcinogenesis in otherwise microscopically/histologically normal-appearing cells. These data indicate that this advance in single-cell optics represented by PWS may have significant biomedical applications.

light-scattering spectroscopy | nanoarchitecture | subdiffusion

Existing knowledge of changes in cell architecture in disease processes is based to a large degree on the histological examination of cells and tissue. On the other hand, it is well accepted that histological and, thus, microarchitectural, aberrations are preceded by molecular, genetic, or epigenetic changes. One may pose a question whether these events are still accompanied by alterations in cell architecture that are histologically undetectable. Indeed, the diffraction limit restricts the resolution of conventional light microscopy to, at best, 200 nm. This is larger than the sizes of the fundamental building blocks of the cell, such as membranes, cytoskeleton, ribosomes, and nucleosomes. Thus, conventional light microscopy is insensitive to changes in nanoarchitecture, which is the fundamental basis of cell organization. It is clear that the fact that a cell is histologically normal may not necessarily be equated with the cell not having nanoscale structural alterations.

Cellular alterations in carcinogenesis provide an illustrative and practically important example. The process of carcinoma formation involves stepwise accumulation of genetic and epigenetic alterations in epithelial cells over a time period of many years. Dysplasia, or structural alterations detectable by microscopy, is a relatively late event in this process. From a cancer-research perspective, it is important to recognize the earlier stages of carcinogenesis that precede histological changes. One can hypothesize that although these genetic/epigenetic aberrations have not yet resulted in histologically apparent changes, they may still be accompanied by architectural consequences that occur at the nanoscale.

Therefore, it is of major importance to design optical techniques for inspecting cell nanoarchitecture. One approach to probe cell architecture has been through the use of spectral analysis of light scattering (1–4). This premise is based on the fact that the spatial variation of the concentration of intracellular solids (e.g., proteins, DNA, RNA, lipids) gives rise to spatial fluctuations in the refractive index of the tissue. However, light scattered by cells and tissues is typically recorded after its 3D propagation within tissue. As a result, although light scattering does depend on a wide range of length scales of refractive index fluctuations including those smaller than the wavelength of light, the sensitivity to subwavelength length scales decreases fast with size because of the Fourier-transform relationship between the scattering signal and the scattering potential (5).

On the other hand, if photons propagating in 1D are recorded, a completely different scenario emerges. According to mesoscopic light transport theory (6–11), the reflected signal in 1D, which is the result of the multiple interference of light waves reflected from refractive index fluctuations, is non-self-averaging* for all length scales for weak refractive index fluctuations (6–8, 12). In other words, the reflected signal is sensitive to any length scale of refractive index fluctuations including those below the wavelength (13–16). This presents an opportunity to characterize cell nanoarchitecture by detecting waves propagating in 1D. This, however, has not been feasible by using conventional far-field microscopy or light-scattering techniques.

Here, we present a type of microscopic spectroscopy, referred to as partial-wave spectroscopy (PWS). PWS detects 1D-propagating back-scattered photons in the far field. Mesoscopic theory-based analysis of the spectra of the resulting signals quantifies the statistical properties of the nanoarchitecture of living or fixed cells. In this article, as an illustration of the efficacy of PWS, we apply this technique to study nanoarchitectural alterations in the process of colon carcinogenesis that precede histological changes. Our approach is to assess alterations in colon cells undergoing defined genetic modulations that are biologically significant but fail to result in abnormalities detectable by conventional microscopy. Specifically, we used RNAi in the human colorectal cancer cell line (HT-29) to test the effect of a modest (≈30–50%) suppressor of the gene C-terminal src kinase (CSK) and a protooncogene, epidermal growth factor

Author contributions: P.P., Y.L., A.T., and V.B. designed research; H.S. performed research; P.P., Y.L., I.R.C., X.L., J.D.R., A.H., D.K., H.K.R., A.T., and V.B. contributed new reagents/analytic tools; H.S., P.P., I.R.C., and X.L. analyzed data; and H.S., P.P., and V.B. wrote the paper.

The authors declare no conflict of interest.

This article is a PNAS Direct Submission.

[1]To whom correspondence may be addressed. E-mail: hariharan@u.northwestern.edu or v-backman@northwestern.edu.

*In a self-averaging system the standard deviation of a parameter relative to its mean decreases with increase in system size, typically as the square root of the system size. On the contrary, in a non-self-averaging system the standard deviation of a parameter relative to its mean increases with increase in system size.

This article contains supporting information online at www.pnas.org/cgi/content/full/0804723105/DCSupplemental.

receptor (EGFR), proteins implicated in early colon carcinogenesis. After this, we used a mouse model in which the *adenomatous polyposis coli* (*APC*) gene underwent a germ-line mutation, the initiating genetic event in ≈80% of human colon carcinomas. We report that, although these molecular events do not result in histologically detectable changes in cells, PWS imaging demonstrated profound alterations in the statistical properties of cell nanoarchitecture. This has future applications in early diagnosis of cancer.

Results

Partial-Wave Spectroscopy (PWS). The design of the PWS instrument is discussed in *Methods*. A focused wave of broadband, low-spatially-coherent light (spatial coherence length is in the order of the diffraction limit, ≈700 nm in our case) illuminates a sample, and an image formed by back-scattered photons is acquired in the far field. The spectrum of the back-scattered light intensity from 390 to 750 nm is recorded for each pixel of the image with 3-nm resolution. PWS combines certain aspects of microscopy and the spectroscopy of light elastically scattered by cells. However, unlike conventional microscopy, in which an image is formed by integrating the reflected or transmitted intensity over a broad spectrum, PWS measures spectral fluctuations in the back-scattering spectra. Unlike elastic scattering spectroscopy, where a signal is formed by the far-field interference of all waves propagating within a scattering particle, the spectrum analyzed in PWS is formed by a subset of these waves (i.e., "partial waves").

PWS virtually divides a cell into a collection of parallel channels each with a diffraction-limited transverse size, detects back-scattered waves propagating along 1D trajectories within these channels, and quantifies the statistical properties of the nanoarchitecture of a cell by the analysis of the fluctuating part of the (normalized) reflected intensity $R(\lambda, x, y)$, where λ is the wavelength of light, and x and y are the spatial coordinates of a particular channel. The spectral fluctuations in $R(\lambda, x, y)$ arise from the interference of photons reflected from refractive index fluctuations within a scattering object, e.g., the cell. Although the lateral size of each channel is determined by the diffraction-limited resolution of the imaging system, information about refractive index fluctuations at subwavelength scales along the channel is imbedded into R. The spectral fluctuations are analyzed by means of 1D mesoscopic light transport theory (6–11), which calculates a disorder strength $L_d(x, y) = \langle \Delta n^2 \rangle l_c$ (following terminology used in the condensed matter physics) for each channel (x, y), where $\langle \Delta n^2 \rangle$ is the variance of refractive index fluctuations Δn within a channel, and l_c is the spatial correlation length of these refractive index fluctuations.

Therefore, a 2D map of the disorder strength $L_d(x, y)$ depicts the spatial distribution of the degree of disorder in the cell under analysis. In practice, it is convenient to quantify a particular cell or a group of cells by a finite number of parameters, rather than an entire 2D image. For example, a cell can be characterized by 2 convenient statistics: the mean intracellular disorder strength $L_d^{(c)}$ (i.e., $L_d(x, y)$ averaged over x and y) and the intracellular standard deviation $\sigma^{(c)}$ of $L_d(x, y)$. The averages of $L_d^{(c)}$, $\sigma^{(c)}$ over a group of cells, such as all cells from a particular cell line or a particular patient, are termed the group means $L_d^{(g)}$ and $\sigma^{(g)}$.

The disorder strength quantifies the spatial variability of refractive index and, thus, the local concentration of intracellular material. At a given point in a cell, Δn is proportional to the local concentration of intracellular solids (17, 18), whereas l_c can be viewed as the characteristic size of the intracellular ultrastructure of a cell (e.g., macromolecular "building blocks" of a cell).

We have confirmed the dependence of L_d, as measured by PWS, on nanoscale refractive index fluctuations by conducting rigorous numerical experiments using finite-difference time-domain (FDTD) simulations (l_c from 5 to 45 nm) and experiments with deterministic nanostructured model media (l_c from 20 to 125 nm). Both sets of experiments are discussed in supporting information (SI) *Text*. Importantly, these studies demonstrated that, in principle, there is no limitation on the minimum l_c that can be assessed by PWS, in contrast to conventional microscopy, which is limited by the diffraction limit of the system. (In practice, of course, the limit of sensitivity to l_c is determined by the signal-to-noise ratio.)

Experiments with Cell Lines. To demonstrate the ability of PWS to identify nanoarchitectural changes in cells that are otherwise histologically indistinguishable, we performed our first set of experiments on HT29 human colonic adenocarcinoma cell line. We focused on colorectal cancer, given that it is a major public health problem (second leading cause of cancer deaths in Western countries). The choice of this model was based also on the fact that the malignant behavior of the HT29 cells can be controlled by genetic modification of these cells (19–21). We selected the tumor suppressor gene CSK and the protooncogene, EGFR. We constructed stable Sh-RNA in HT-29. Thus, we used 3 variants of HT29 cells: original HT29 cell line transfected with empty vector, HT29 cells after CSK knockdown, which leads to increased malignant aggressiveness, and the cells after EGFR knockdown, which partially suppresses the malignant aggressiveness of the cell line (discussed in *SI Text*). We noted, as expected, that CSK knockdowns behave more aggressively, whereas EGFR was less aggressive, using proliferation (proliferating cell nuclear antigen) as a surrogate marker (Fig. S1). Importantly, as demonstrated in previous literature (19–21), the 3 cell lines are microscopically/histologically indistinguishable, which was further corroborated by a pathologist examining the stained cytological preparations of these cells. This is related, at least partly, to the relatively modest knockdown achieved (≈30–50%), meaning that the magnitude of genetic alterations were insufficient to cause microscopic alterations but did result in the modulation of cellular physiology such as proliferation (CSK ShRNA > HT-29 empty vector > EGFR ShRNA).

PWS measurements were conducted on ≈50 cells randomly selected from each of the 3 cell types (≈500 1D channels per cell). The protocol for PWS measurements and signal analysis are discussed in *Methods* and illustrated in Fig. 1. Three major conclusions can be made from the inspection of Fig. 1 (*A–E*). First, *A*, *B*, and *C* illustrate that PWS signals are in agreement with 1D mesoscopic theory (see *Methods* for detail). The second conclusion is that PWS enables sensing architectural changes in otherwise histologically indistinguishable but genetically and physiologically different cells. Fig. 1 *D* and *E* compares H&E and PWS images of 3 representative cells from the 3 cell lines: control HT29, EGFR knockdown, and CSK knockdown cells. As can be seen from the images, the 3 representative cells appear cytologically similar. This was also confirmed by the analysis of at least 10 cells from each of the cell line. For comparison, PWS images are clearly different. Overall, a cell from the most aggressive cell line (CSK knockdown) has the highest intracellular disorder strength, whereas the least aggressive cell line (EGFR knockdown) exhibits the least disorder. This suggests that a higher-disorder strength is associated with an increased malignant behavior. Fig. 1*E* also shows a PWS image of a glass slide with no cells to illustrate the noise level in L_d images: The disorder strength of the pure glass is negligible compared with L_d of cells and is spatially uniform, as expected. This further validates that PWS is sensitive to nanoscale refractive index fluctuations given the current signal-to-noise ratio.

Fig. 1*F* plots intracellular averages of disorder strength vs. its intracellular standard deviation $L_d^{(c)}$ vs. $\sigma^{(c)}$ for all cells for the 3 cell lines with each cell being represented by a single point: $[L_d^{(c)}, \sigma^{(c)}]$. Clearly, $L_d^{(c)}$ and $\sigma^{(c)}$ parallel increased malignant potential of the cell lines. This is further illustrated by Fig. 1 *G* and *H*,

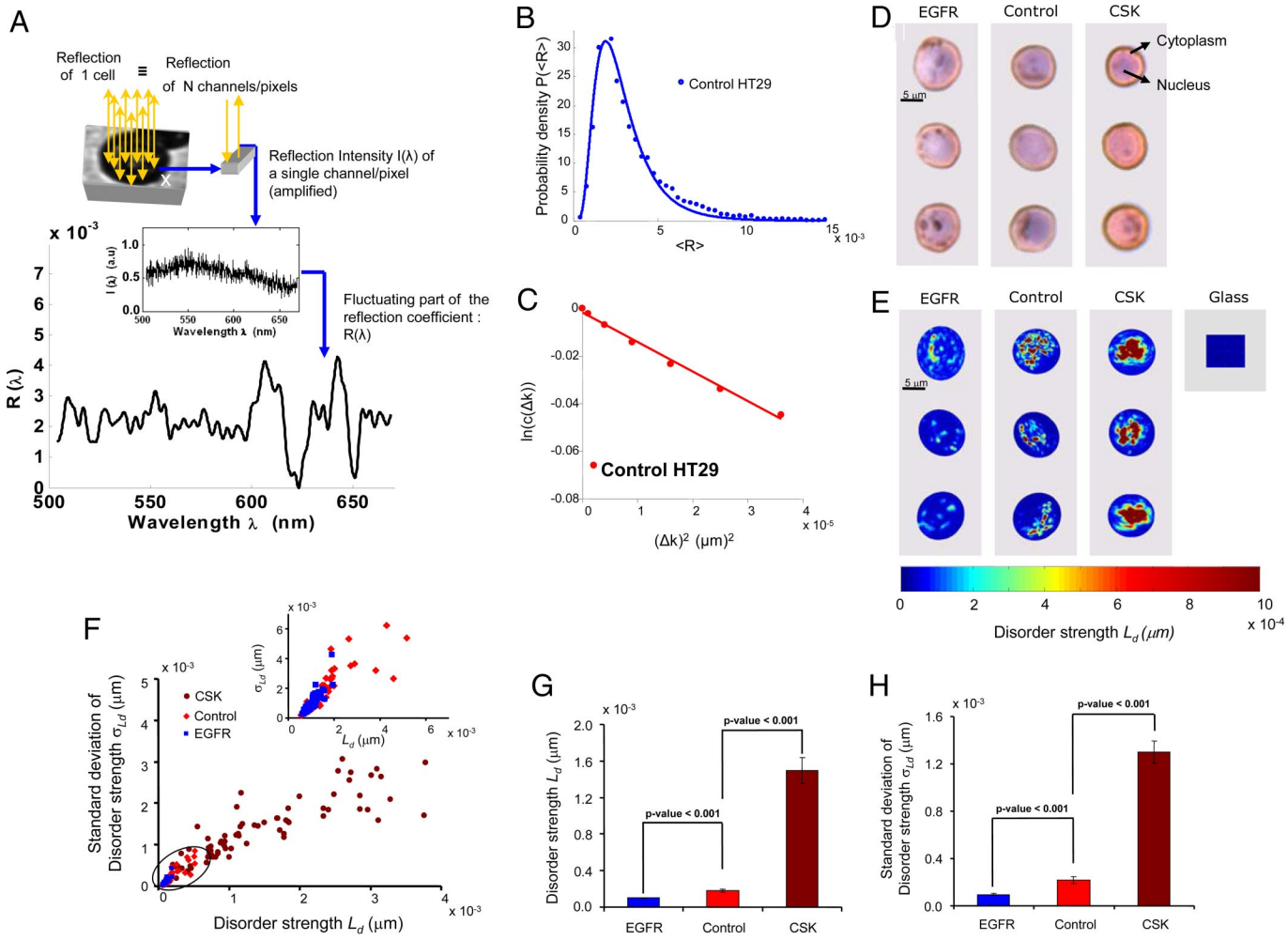

Fig. 1. PWS detects architectural changes in genetically modified HT29 cell lines that are otherwise histologically indistinguishable. (*A*) Steps involved in PWS signal acquisition and analysis. The spectrum of a typical reflection coefficient $R(\lambda)$ obtained after removing the noise and the background reflection. (*Inset*) A typical back-scattering spectrum $I(\lambda)$ from a single pixel of an HT29 cell image. (*B*) A representative p.d.f. $P(<R>)$ of the mean fluctuating component $\langle R \rangle$ (circles) in HT29 cells. The solid lines are the fitted $P(R)$ curve that follows the log-normal distributions ($r^2 > 0.95$). (*C*) The representative correlation decay $C(\Delta k)$ computed from $R(k)$. The logarithm of the autocorrelation function $\ln(C(\Delta k))$ (circles) follows a linear dependence on $(\Delta k)^2$ (solid line) ($r^2 = 0.98$). (*D*) Representative cytological images (H&E staining) from 3 variants of HT29 cells. The nucleus and cytoplasm of a cell is marked for reference. The cytology images look similar for all of the 3 types of cells. (*E*) The representative pseudocolor PWS images from the 3 cell types shown in *D*: Color shows the magnitude of the L_d in a cell. These representative cells are chosen such that they correspond to the average L_d for each cell type. Each color map shows the entire cell. Although the cytology images shown in *D* appear similar, the PWS images are distinctly different from each other. To see the noise level, we also provide an L_d image of a pure glass that shows very low L_d relative to those of the cells. It is important to note that the HT29 cell, as an adenocarcinoma cell line, is dominated by a large nucleus. Hence, the PWS images indicate that the disorder is increased in the cell nucleus. However, the changes in disorder are not localized in the nucleus only and are present throughout the cytoplasm as is seen in cells with small nucleus-to-cytoplasm ratio. (*F*) Cells with a more aggressive malignant behavior have a higher intracellular disorder strength. The values of L_d and σ_{Ld} averaged over a cell, that is $L_d^{(c)}$ and $\sigma^{(c)}$, from 3 variants of HT29 cells plotted in $L_d^{(c)}$,$\sigma^{(c)}$ parameter space. As can be seen, for each cell type there is a separate regime in the parameter space that only slightly overlaps with the regimes of the other cell types. (*Inset*). The part of the parameter space for the EGFR and control HT29 cells with small L_d and σ_{Ld} values is amplified to show their separation in the parameter space. (*G*) The relative values of $L_d^{(g)}$ from 3 variants of HT29 cells. The error bar represents the standard error of the mean. The average $L_d^{(g)}$ is significantly decreased for the least-aggressive EGFR-knockdown cells compared with that of HT29 cells ($P < 0.001$) and significantly increased for the most-aggressive CSK-knockdown cells ($P < 0.001$). (*H*) The values of $\sigma^{(g)}$ for the 3 cell types. $\sigma^{(g)}$ is progressively increased from the least-aggressive EGFR-knockdown, to the control and to the most-aggressive CSK-knockdown cells (all P values < 0.001).

which shows that $L_d^{(c)}$ and $\sigma^{(c)}$ are progressively and highly statistically significantly increased from EGRF knockdown to control HT-29 and to CSK knockdown cell lines (ANOVA P value <0.001). We also point out that, intriguingly, there is a certain degree of intercellular heterogeneity among cells belonging to the same cell line as illustrated by a spread of data points in the $L_d^{(c)}$ vs. $\sigma^{(c)}$ plot. The intercellular heterogeneity appears to be the highest for the most aggressive CSK-knockdown cells. We note that despite partial overlap among cells from different groups, it was still possible to differentiate the 3 cell lines by analyzing a group of cells. For example, to achieve a statistical power of 90%, the dataset shown in Fig. 1*F* required 23 cells to differentiate EGFR vs. control HT29 cells and 15 cells to differentiate CSK vs. control HT29 cells.

Experiments with the Animal Model of Colon Carcinogenesis. Based on our cell line studies, we hypothesized that the degree of disorder of cell nanoarchitecture correlates with the neoplastic behavior and can be used as a marker of carcinogenesis. We wanted to test this hypothesis in animal studies. We used 1 of the best-validated models of intestinal carcinogenesis, the MIN mouse. In this model, there is a truncation in the *APC* tumor

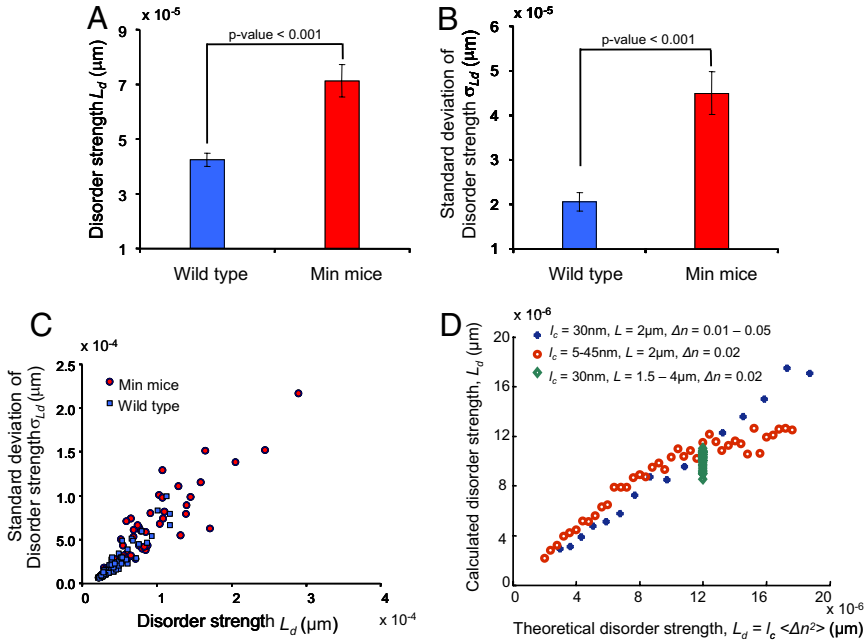

Fig. 2. Histologically normal-appearing precancerous cells from the MIN-mouse model of intestinal carcinogenesis possess alterations in their nanoarchitecture detectable by PWS. (*A*) The bar graph shows that the $L_d^{(g)}$ is significantly increased in the precancerous cells obtained from the MIN mice relative to that of the control wild-type animals ($P < 0.001$). (*B*) Comparison of $\sigma^{(g)}$ in the wild-type and MIN mice. There is a significant increase in $\sigma^{(g)}$ ($P < 0.001$) for the MIN mice compared with the control wild-type animals. (*C*) L_d and σ_{Ld} averaged over a cell [i.e., $L_d^{(c)}$ and $\sigma^{(c)}$] for the cells obtained from the wild-type and the MIN-mice plotted in the $[L_d^{(c)},\sigma^{(c)}]$ parameter space. Each point in this diagram corresponds to a single cell. Both the wild-type and MIN-mice cells have a separate regime in the parameter space with slight overlaps. (*D*) Comparison of the theoretical (true) $L_d(L_d\langle\Delta n^2\rangle l_c)$ and the one calculated by using Eqs. **1** and **2** based on the FDTD simulations of light reflection from a 1D weakly disordered random media. The simulations were performed on a homogeneous dielectric slab with random additive refractive index fluctuations around the background refractive index $n_0 = 1.38$. L_d was obtained for the following parameters: (*i*) standard deviation of the refractive index fluctuations Δn between 0.01 and 0.05, (*ii*) the correlation length l_c between 5 and 45 nm, and (*iii*) the thickness of the sample L between 1.5 and 4 μm. As can be seen, the calculated and theoretical values of L_d agree well with each other ($r^2 = 0.91$), thereby confirming its agreement with the mesoscopic theory.

suppressor gene (codon 850), which results in spontaneous development of intestinal adenomas. Importantly, given the germ-line nature of the mutation, all intestinal epithelial cells (including those that were histologically normal) contained the mutation in this tumor suppressor gene. The relevance of this mutation is underscored by the observation that ≈80% of sporadic colorectal cancers are believed to be initiated by *APC* truncation.

The question we asked was as follows: Although appearing normal by the criteria of microscopic histopathology, do precancerous intestinal cells possess alterations in their nanoarchitecture that are detectable by PWS? In our studies, we used 4 C57 Bl male wild-type mice (negative control) and 4 age-matched male C57BL *APC*min animals. The mice were killed at the age of 15 weeks, and intestines were washed. Samples were taken from visually normal mucosa by using a cytology brush. Care was taken to avoid any possibility of contamination with adenomas through examination with a dissecting microscope of dry ice-treated epithelium. The wild-type animal intestines were treated identically. Cells from the cytology brush were smeared onto a glass slide and alcohol-fixed according to a standard protocol (discussed in *SI Text*). For each mouse, ≈30 cells were randomly chosen for PWS analysis. All cells were obtained from the macroscopically and histologically normal mucosa outside any neoplastic lesion. The cytology specimens were then examined by a surgical pathologist, who confirmed that all cells were histologically normal.

Fig. 2 *A–C* shows that both $L_d^{(c)}$ and $\sigma^{(c)}$ are highly significantly ($P < 0.001$) increased in the cells from the MIN mice compared with those from wild-type mice, in agreement with the findings of the cell-line study. Thus, we conclude that the germ-line mutation in otherwise microscopically normal-appearing cells results in the increase in the disorder of cell nanoarchitecture.

It has to be pointed out that although cells obtained from the same animal exhibit a certain degree of intercellular variability in their $L_d^{(c)}$ and $\sigma^{(c)}$, these parameters are quite well conserved among cells from different parts of the intestine and even different mice. The intercellular standard deviation of $L_d^{(c)}$ for control animals is <15% of its mean, $L_d^{(g)}$. For comparison, this intercellular variability of $L_d^{(c)}$ increases in MIN mice up to ≈50%. This suggests that the population of precancerous cells is significantly more heterogeneous compared with the cells from control animals. The biological significance of this finding remains to be explored.

Length Scale Probed by PWS. Because L_d is a product of Δn and l_c, it is impossible to determine l_c explicitly. However, an approximate value of l_c can be estimated. For Δn ranging between 0.02 and 0.10, which is typical for a biological tissue (22), the experimentally measured values of L_d for the cell lines and mice cells correspond to l_c less than or ≈100 nm. This is the length scale of the fundamental "building blocks" of the cell, such as protein complexes, cytoskeleton, intracellular membranes, and nucleosomes. It needs to be emphasized that l_c is not a mere size of a particular cell structure but instead characterizes the statistical properties of the entire complexity of the intracellular refractive index fluctuations.

Discussion

PWS provides a unique way of isolating 1D back-scattering photons, which are sensitive to minute changes in the refractive index fluctuations at subdiffractional length scales. Combined

with mesoscopic light transport theory for statistical analysis of the back-scattered photons, PWS provides a unique statistical view of subcellular architecture at nanoscale beyond what conventional microscopy reveals. In particular, PWS measures the disorder strength, a statistical parameter of the complex refractive index fluctuations at a single-cell level.

We demonstrate that PWS has the ability to provide unprecedented detail about the nanoscale architecture of a cell. This was validated in studies where defined genetic alterations were introduced both in vitro and in vivo and the disorder consequences were assessed in histologically normal cells. In the in vitro study, PWS was used to image cells from 3 genetic variants of HT29 colon human tumor cell line (original HT29 cell line and EGFR and CSK knockdowns). Although microscopically indistinguishable, these 3 types of cells exhibit different degree of malignant behavior, from less aggressive (EGFR knockdown) to more aggressive (CSK knockdown). Our results demonstrate that PWS was able to differentiate cells from these lines by quantifying the disorder of cell nanoarchitecture. In particular, the increase in malignant aggressive behavior was associated with the increase in the disorder strength of intracellular organization. The increase in the disorder of cell architecture was further confirmed in the study with the MIN-mouse model of intestinal carcinogenesis. Again, the same trend was observed: A germ-line mutation in intestinal epithelial cells in the MIN mice that were normal-appearing by conventional histologic standards resulted in a profound increase in the disorder strength compared with the control mice. This suggests that early carcinogenesis is accompanied by increasing disorder and progressively higher heterogeneity of the intracellular nanoarchitecture.

These results may have profound biological and medical implications. From the cancer-biology perspective, PWS may be used to better understand early cellular events in carcinogenesis. Cell architecture may be much more "in tune" with the molecular events than previously thought. Although it may not be possible at this point to identify which specific structures are responsible for the increase in the disorder and associated molecular mechanisms, we can get some insights into the kinds of nanoscale changes developing in preneoplastic cells. Because $L_d = \langle \Delta n^2 \rangle l_c$, a higher disorder strength is due to the increase in the refractive index fluctuations Δn^2, or refractive index correlation length l_c. A higher Δn^2 may be associated with the increased spatial variation of the density of intracellular material (e.g., DNA, RNA, proteins and lipids) (17, 18). As discussed in *Results*, $l_c \approx 100$ nm. Thus, a change in l_c may represent aggregation or "packing" of some of the basic "building blocks" of the cell. Similarly, the increase in l_c can be related to the increase in fractal dimension reported by other groups (1) and also to the log-normal size distribution of particles (23, 24), where the increase in l_c would indicate the increase in the average and standard deviation of the log-normal distribution. Furthermore, our data also suggest that the increase in the disorder strength is not limited to a specific organelle or a type of molecule. Instead, it represents the progression of global intracellular organization toward a more disordered state.

From the clinical perspective, our data indicate that PWS has the potential to detect cell changes that would otherwise be missed by conventional histopathology. PWS may potentially provide another dimension to histopathology and complement and expand its use. Moreover, PWS could be useful to detect field carcinogenesis in organs such as the colon providing a potential means of using easily accessible normal-appearing mucosa to determine the risk of neoplasia throughout the colon without the need for interrogation of a formed dysplastic lesion. This may also be applicable to other cancer sites where field carcinogenesis is known to be important (e.g., lung, breast, etc.). If the results are confirmed in humans, we may have to redefine our understanding of the significance of cell architecture and what we consider to be a "histologically normal" cell.

Methods

PWS Instrument. The design of the PWS instrument is shown in Fig. S2. The white light from Xe lamp (100 W; Oriel) was collimated by a 4f-lens relay system (≈0.8° divergence angle) and focused onto a sample by a low numerical aperture objective (Edmund Optics, NA ~ 0.4) with the illumination beam diameter of ≈120 μm. At the sample level, the illumination beam was much larger than the sample size (i.e., micron-sized biological cell), had spatial coherence length <1 μm, and was well-collimated (with respect to the size and curvature of a single cell). The back-scattered image was projected on the slit of the imaging spectrograph coupled with the CCD camera and mounted on a motorized 1D linear scanning stage (Zaber Technologies). The image was acquired by scanning the slit of spectrograph in the horizontal direction. In each scanning step, the CCD camera records a matrix with the vertical axis corresponding to a spatial position of the image and the horizontal axis corresponding to the wavelength of light, λ. Therefore, the instrument acquired back-scattering spectra $I(\lambda, x, y)$ (λ = 390–750 nm, 1,392 wavelengths, spectral resolution ≈3 nm) for each pixel (x, y) on the image. All spectra were normalized by the spectra of the incident light.

$I(\lambda, x, y)$ were further analyzed (see the following section) to calculate the fluctuating component of these back-scattering spectra, $R(k, x, y)$ (k is the wave number) that arises from the interference of photons reflected from refractive index fluctuations within a scattering object. Because of weak refractive index fluctuations existing in biological cells and the low spatial-coherence illumination, this detection scheme isolates photons localized in 1D. In essence, PWS decomposes a complex 3D weakly disordered medium into many spatially independent parallel 1D channels and acquires 1D reflection spectra $R(k)$ originating because of the interference of photons propagating in these 1D channels. The condition of the weak scattering within the medium and the low-coherence illumination essentially prevents the interference of the back-scattered light emerging from different 1D channels (Fig. S3). Although the lateral size of each channel is determined by the diffraction-limited resolution of the system (≈700 nm), information about refractive index fluctuations at subwavelength scales is imbedded into $R(k)$.

Calculation of Fluctuating Component $R(k)$ from the Back-Scattering Signal. $R(k)$ was computed from $I(k)$ for each pixel in a cell image. This was accomplished in 3 steps. First, we filtered out the high-frequency noise by using a 6th-order low-pass Butterworth filter with a normalized cutoff frequency of 0.08. The determination of the amplitude and the normalized cutoff frequency is discussed in *SI Text*. The result was a noise-filtered spectrum $I(k)$. Second, a low order polynomial $[I_p(k)]$ was fit to $I(k)$. Third, $R(k)$ was obtained as $R(k) = I(k) - I_p(k)$.

Calculation of Disorder Strength by Using Mesoscopic Light-Transport Theory. Because $R(k)$ is formed primarily by 1D back-scattered photons, $R(k)$ can be analyzed by means of the 1D mesoscopic light-transport theory in disordered media (6–11). This theory has been well-studied and used for electron transport in conductors and light transport in dielectric media. The mesoscopic theory enables quantification of the statistical properties of the spatial refractive index variations within a 1D scattering medium, e.g., a 1D channel within a cell. A corresponding measurable statistical parameter obtained for each channel is the disorder strength $L_d = \alpha \langle \Delta n^2 \rangle l_c$ (following terminology used in the condensed-matter physics), where $\langle \Delta n^2 \rangle$ is the variance of refractive index fluctuations Δn within a channel, l_c is the spatial correlation length of these refractive index fluctuations, and α is a numerical factor ≈1.

One can determine L_d for each pixel in a cell image from 2 experimentally acquired quantities: $R(k)$ and its autocorrelation function $C(\Delta k) = \langle R(k)R(k + \Delta k) \rangle / \langle R(k)R(k) \rangle$ (6–11). In a weakly disordered medium (i.e., $R \ll 1$), the probability density distribution of R is log-normal for all length scales of the disordered scattering medium (8, 9, 12). The ensemble average of the R distribution over the ensemble of 1D independent parallel disordered channels $\langle R \rangle \cong \frac{1}{2}[\exp(4k^2 L_d L / n_0^2) - 1)]$, where n_0 is the average refractive index of the medium, and L is the longitudinal (i.e., along the direction of incident light propagation) dimension of the medium. If $kl_c \ll 1$ and $4k^2 L_d L / n_0^2 \ll 1$,

$$\langle R \rangle \cong 2k^2 L_d L / n_0^2. \quad [1]$$

(8, 9, 12, 23). Furthermore, $C(\Delta k) \cong \exp[-(\Delta k)^2 f(l_d) AL]$, where $f(L_d)$ is a slowly varying function for realistic values of the disorder strength and is neglected in the following analysis. Thus,

$$\ln(C(\Delta k)) = -(\Delta k)^2 AL, \quad [2]$$

where A is a constant (12, 25). Therefore, knowing $\langle R \rangle$ and $C(\Delta k)$ for each channel in a cell, one can calculate L_d by eliminating L.

Calculation of L_d in Biological Cells. For each 1D channel, the mean fluctuating component $\langle R \rangle$ was calculated by taking the root mean-square average of $R(k)$ over a spectral range from $\lambda_m = 500$ nm to 660 nm (outside this range the intensity of the spectrum drops below the noise floor and hence was not included in our analysis). Because $C(\Delta k)$ is a function of k, $C(\Delta k)$ was calculated for k corresponding to the middle of the spectrum 580 nm for a better spectral averaging and for the full use of the spectra in the calculation.

Fig. 1 illustrates the steps involved in obtaining a PWS image of a cell. The instrument measured the total back-scattering signal $I(\lambda, x, y)$ for each point (x, y). The next step is to extract $R(\lambda, x, y)$ from $I(\lambda, x, y)$ as discussed above. A representative $R(\lambda)$ from a single channel within a HT29 cell is shown in Fig. 1*A*. Then $C(\Delta k, x, y)$ is calculated from $R(k, x, y)$. A representative example of $C(\Delta k)$ for a HT29 cell is shown in Fig. 1*B*. For each channel (x, y), disorder strength $L_d(x, y)$ was computed from $R(k, x, y)$ and $C(\Delta k, x, y)$ by using Eqs. **1** and **2**. Three representative pseudocolor disorder-strength images for HT29, CSK, and EGFR cells are shown in Fig. 1*E*.

Experimental Validation of Nanoscale Sensitivity of PWS. We performed 3 studies to validate nanoscale sensitivity of PWS: (*i*) rigorous computational experiments, (*ii*) experiments with nanostructured models, and (*iii*) experiments with biological cells. These studies are discussed in detail in *SI Text*. In brief, our computational experiments were based on finite-difference time-domain (FDTD) (26) simulations of light propagation in random cell-emulating media with controlled refractive index distributions (l_c varied from 5 to 45 nm). As shown in Fig. 2*D*, the values of L_d determined based on the spectral analysis were in good agreement with the true value ($r^2 = 0.91$). A key result is that L_d linearly depends on l_c for $kl_c < 1$. Thus, in principle, there is no limitation on the minimum l_c that can be assessed by this method. In our experiments with deterministic nanostructured model media, the models comprised aggregated polystyrene nanospheres of known sizes ($l_c = 20$ to 125 nm) (27). We found a good agreement ($r^2 = 0.97$) between L_d measured by using the PWS instrument and the expected disorder strengths. This experiment also served the purpose of calibrating the system.

Finally, we wanted to obtain evidence that our mesoscopic theory-based analysis is valid for real biological cells. Luckily, retrospective analysis of the data (*R* and *C*) could be used to validate the analysis. Indeed, the analysis is applicable if 3 conditions are satisfied: (*i*) $\langle R \rangle \ll 1$, (*ii*) the probability distribution function (p.d.f.) of $\langle R \rangle$ is log-normal, and (*iii*) $C(\Delta k)$ is a Gaussian function. Fig. 1 shows that these 3 conditions are satisfied. (*i*) The fact $\langle R \rangle \ll 1$ is clear from Fig. 1*A*. (*ii*) Fig. 1*B* shows a representative p.d.f. of $\langle R \rangle$ for the ensemble of all HT29 cells. This p.d.f. is well-approximated by the log-normal function ($r^2 > 0.95$). (*iii*) Finally, as illustrated in Fig. 1*C*, $C(\Delta k)$ is well-approximated by a Gaussian function (average $r^2 = 0.98$ for a linear fit to ln $C(\Delta k)$ vs. Δk^2 for the ensemble of all HT29 cells). This indicates that our experimental cell data indeed conforms to the 1D mesoscopic theory.

ACKNOWLEDGMENTS. This work was supported in part by National Institutes of Health Grants R01 EB003682, R01 CA112315, and R01 CA128641 and National Science Foundation Grant CBET-0733868. A.H. was supported in part by the Canary Foundation/American Cancer Society Early Detection Postdoctoral Fellowship.

1. Wax A, *et al.* (2002) Cellular organization and substructure measured using angle-resolved low-coherence interferometry. *Biophys J* 82:2256–2264.
2. Perelman LT, *et al.* (1998) Observation of periodic fine structure in reflectance from biological tissue: A new technique for measuring nuclear size distribution. *Phys Rev Lett* 80:627–630.
3. Mourant JR, *et al.* (1995) Spectroscopic diagnosis of bladder cancer with elastic light scattering. *Laser Surg Med* 17:350–357.
4. Sokolov K, Drezek R, Gossage K, Richards-Kortum R (1999) Reflectance spectroscopy with polarized light: Is it sensitive to cellular and nuclear morphology. *Optics Express* 5:302–317.
5. Born M, Wolf E (1999) *Principles of Optics: Electromagnetic Theory of Propagation, Interference and Diffraction of Light* (Cambridge Univ Press, Cambridge, UK).
6. Anderson PW, Thouless DJ, Abrahams E, Fisher DS (1980) New method for a scaling theory of localization. *Phys Rev B* 22:3519–3526.
7. Abrikosov AA, Ryzhkin IA (1978) Conductivity of quasi-one-dimensional metal systems. *Adv Phys* 27:147–230.
8. Kumar N (1985) Resistance fluctuation in a one-dimensional conductor with statis disorder. *Phys Rev B* 31:5513–5515.
9. Rammal R, Doucot B (1987) Invariant imbedding approach to localization. 1. General framework and basic equations. *J Phys (Paris)* 48:509–526.
10. Pradhan P, Kumar N (1994) Localization of light in coherently amplifying random-media. *Phys Rev B* 50:9644–9647.
11. Haley SB, Erdos P (1992) Wave-propagation in one-dimensional disordered structures. *Phys Rev B* 45:8572–8584.
12. Anderson PW (1958) Absence of diffusion in certain random lattices. *Phys Rev* 109:1492–1505.
13. Lee PA, Ramakrishnan TV (1985) Disordered electronic systems. *Rev Mod Phys* 57:287–337.
14. Abrahams E, Anderson PW, Licciardello DC, Ramakrishnan TV (1979) Scaling theory of localization—Absence of quantum diffusion in two dimensions. *Phys Rev Lett* 42:673–676.
15. Kramer B, Mackinnon A (1993) Localization—theory and experiment. *Rep Prog Phys* 56:1469–1564.
16. Mott NF, Twose WD (1961) The theory of impurity conduction. *Adv Phys* 10:107–163.
17. Barer R, Tkaczyk S (1954) Refractive index of concentrated protein solutions. *Nature* 173:821–822.
18. Kekicheff P, Laughlin RG, Munyon RL (2001) Diffusive interfacial transport: A new approach to concentrated protein solution studies. *Langmuir* 17:4693–4696.
19. Kunte DP, *et al.* (2005) Down-regulation of the tumor suppressor gene C-terminal Src kinase: An early event during premalignant colonic epithelial hyperproliferation. *FEBS Letters* 579:3497–3502.
20. Roberts RB, *et al.* (2002) Importance of epidermal growth factor receptor signaling in establishment of adenomas and maintenance of carcinomas during intestinal tumorigenesis. *Proc Natl Acad Sci USA* 99:1521–1526.
21. Van Slyke P, *et al.* (2005) Dok-R mediates attenuation of epidermal growth factor-dependent mitogen-activated protein kinase and Akt activation through processive recruitment of c-Src and Csk. *Mol Cell Biol* 25:3831–3841.
22. Schmitt JM, Kumar G (1998) Optical scattering properties of soft tissue: A discrete particle model. *Appl Opt* 37:2788–2797.
23. Mourant JR, *et al.* (2002) Polarized angular dependent spectroscopy of epithelial cells and epithelial cell nuclei to determine the size scale of scattering structures. *J Biomed Opt* 7:378–387.
24. Wilson JD, Foster TH (2005) Mie theory interpretations of light scattering from intact cells. *Opt Lett* 30:2442–2444.
25. Feng SC, Kane C, Lee PA, Stone AD (1988) Correlations and fluctuations of coherent wave transmission through disordered media. *Phys Rev Lett* 61:834–837.
26. Taflove A, Hagness SC (2005) *Computational Electrodynamics: The Finite-Difference Time-Domain Method* (Artech House, Boston).
27. Chen K, Taflove A, Kim YL, Backman V (2005) Self-assembled patterns of nanospheres with symmetries from submicrons to centimeters *Appl Phys Lett* 86.

Supporting Information

Subramanian *et al.* 10.1073/pnas.0804723105

SI Text

Cell Cultures. EGFR and CSK gene knockdown stable constructs were developed following a conventional protocol. The HuSH EGFR-shRNA vector and the control vector (Origene) and the CSK shRNA vector (BD Biosciences–Clontech) were transfected in colon cancer cell line HT29 by using Lipofectamine 2000 (Invitrogen) according to manufacturer's instructions. After transfection, cells were incubated at 37 °C in a humidified 5% CO_2 incubator. Stable clones for EGFR shRNA and control vector were selected by puromycin (0.5 μg/ml) and the stable clones for CSK shRNA vector were selected by hygromycin (600 μg/ml). The stable clones were confirmed for gene knockdown by RT-PCR and Western blotting by standard methods.

Proliferation of the CSK shRNA and EGFR constructs was determined as follows. Proteins from the stable constructs for CSK shRNA, control vector and the EGFR shRNA were isolated and subjected to Western blotting using standard methods and probed with antibodies against CSK (BD Biosciences), EGFR and PCNA (Both from Santa Cruz Biotechnology) and β-actin (Sigma). We found that stable transfection of the shRNA vectors resulted in 50% decrease in the expression of CSK and EGFR. We have previously shown that CSK down-regulation leads to increased epithelial cellular proliferation. This was evidenced by a significant increase in the proliferation specific marker PCNA in the CSK shRNA construct. EGFR plays an important role in signaling pathways (including cell proliferation) which are implicated in various cancers. Down-regulation of this gene imparts a less proliferating phenotype to the cells. This was confirmed by the dramatic decrease in the proliferation marker PCNA in the EGFR shRNA construct as compared to the control vector.

Animals. All animal studies were performed in accordance with the institutional Animal Care and Use Committee of Evanston–Northwestern Healthcare. Four male C57BL mice (*APC* wild type) and 4 C57BL*APC*min were euthanized at 15 weeks of age. Intestines were removed, opened longitudinally, and flushed with PBS. After that, the intestines were placed on dry ice for 5 min to optimized detection of adenomas. Areas of nondysplastic epithelium were identified by using a dissecting microscope and subjected to gentle treatment with a cytology brush. Cells from the cytology brush were immediately smeared onto a glass microscope slide and the slide was placed in 95% ethanol. The measurements by PWS were taken on isolated colonic cells obtained at random from the colonic mucosa (≈30 cells per animal). We also performed cytological analysis on 10 randomly collected and H&E-stained colonic cells at each time point. The analysis performed by a board-certified pathologist specializing in gastrointestinal cytology confirmed that all cells were histologically normal.

Characteristics of Signal Filter. We estimated the amplitude of the noise and the normalized cutoff frequency (normalized to the sampling frequency—data are sampled every 0.25 nm) from our previous experiments using polystyrene microspheres with known sizes (3). The polystyrene microsphere has no disorder and the back-scattering spectrum is known analytically via Mie theory, thus the noise level was easily distinguishable from the signal. This normalized cutoff for noise filtering also corresponded to the spectral resolution of the instrument and has the following practical implication. The spectral resolution of the instrument is 3 nm. The CCD oversamples a spectrum into 1,392 pixels with a single pixel corresponding to, on average, a 0.25-nm band. (In our experiment, we did not bin the adjacent pixels in the CCD camera to reduce the oversampling. However, we removed all spectral oscillations less than the resolution of the spectrometer by using a low-pass filter.) Because spectral fluctuations with spectral frequencies higher than that of the point spread function can only be attributed to instrument noise, a low-pass filter with normalized cutoff frequency of 0.08 (cutoff frequency/sampling frequency) filters out these spectral fluctuations. Also, varying the normalized cutoff frequency below the spectral resolution does not significantly affect the disorder strength. For example, change in the normalized cutoff frequency from 0.08 to 0.03 (i.e., filters all oscillations <9 nm instead of 3 nm) results in a change in disorder strength of ≈5% which is much smaller than the difference in L_d (≈80%) between EGFR and control cells. On the other hand, if the normalized cutoff frequency is above the spectral resolution, the filter does not completely remove the spectral noise, which may affect the disorder strength. For example, an increase in the normalized cutoff frequency to 0.25 (filters out oscillations under 1 nm instead of 3 nm) results in a 65% change in the disorder strength, as expected.

Validation of PWS in Computational Experiments. We performed numerical simulations of light propagation in random 3D cell-emulating media with controlled refractive index distributions. This was accomplished by using the finite-difference time-domain (FDTD) (1) method which provides an accurate solution for the propagation of light in essentially arbitrary media. The accuracy and robustness of FDTD modeling has been confirmed in multiple previous reports (1). In our simulations, we considered refractive index fluctuations ranging from 0.01 to 0.05 (which is the biologically relevant regime) and correlation lengths l_c ranging from 1 to 100 nm. As shown in Fig. S3, PWS enables isolating 1D-propagating back- scattered waves within the scattering media as demonstrated by the good agreement ($r^2 \approx 0.81$) between PWS spectra calculated by FDTD for any given 1D channel and the spectra calculated for 1D disordered media with the refractive index profile the same as in the given 1D channel (referred to as the 1D-slab model).

Having demonstrated the agreement between the full 3D model and the corresponding 1D model, we performed extensive FDTD simulations for the latter. We considered a homogeneous dielectric slab with random refractive index fluctuations around the background refractive index $n_0 = 1.38$ (similar to the average refractive index of a biological cell). The standard deviation Δn of the fluctuations was varied from 0.01 to 0.05. The correlation length l_c of the fluctuations was defined as $\langle \Delta n(L) \Delta n(L') \rangle \equiv \langle \Delta n^2 \rangle \exp[-|L - L'|/l_c]$, and varied from 5 to 45 nm ($kl_c \ll 1$). The thickness of the sample L was varied from 1.5 to 4 μm. In all cases, L_d was calculated by using Eqs. **1** and **2**. As shown in Fig. 2*D*, the values of L_d determined based on the spectral analysis were in good agreement with the true value ($r^2 = 0.91$), thus confirming the mesoscopic theory based analysis.

A key result of this study is that L_d linearly depends on l_c for $kl_c < 1$. Thus, in principle, there is no limitation on the minimum correlation length that can be assessed by means of the spectral analysis of 1D-propagating photons. In practice, of course, the sensitivity to small l_c is limited by the signal-to-noise ratio and other technical considerations. It should be emphasized, however, that contrary to conventional optical microscopy, the

sensitivity of PWS to small length scales is not bound by a fundamental physical limit.

Validation of PWS by Using Nanostructured Model Media. To calibrate the PWS experimental setup, we performed experiments on a series of nanostructured model media comprised of aggregated polystyrene nanospheres. The models were fabricated using the protocol described in ref. 2. Each model consisted of a self-assembled lattice of aggregated nanospheres of a given size. The refractive index contrast between a polystyrene nanosphere and air modeled refractive index fluctuations. We used nanospheres with sizes 20, 40, 60, 80, 100, and 125 nm. The thickness of the models was varied from 0.3 μm to 13 μm. PWS data were obtained from the total of $\approx$100,000 channels corresponding to 30 different combinations of thickness and nanosphere size. An advantage of this model is that both l_c and Δn are known a priori: l_c corresponds to the size of a nanosphere, and Δn corresponds to the refractive index of a polystyrene sphere relative to air. Thus, it is possible to theoretically estimate the expected disorder strength of a model. There was a good agreement ($r^2 = 0.97$) between the experimentally measured (using PWS instrument) and expected disorder strengths. This experiment also served the purpose of calibrating the system.

1. Taflove A, Hagness SC (2005) *Computational Electrodynamics : The Finite-Difference Time-Domain Method* (Artech House, Boston).
2. Chen K, Taflove A, Kim YL, Backman V (2005) Self-assembled patterns of nanospheres with symmetries from submicrons to centimeters. *Appl Phys Lett* 86.
3. Liu Y, Li X, Kim YL, Backman V (2005) Elastic backscattering spectroscopic microscopy. *Opt Lett* 30:2445–2447.
4. Berenger JP (1994) A perfectly matched layer for the absorption of electromagnetic waves. *J Comput Phys* 114:185–200.
5. Umashankar KR, Taflove A (1982) A novel method to analyze electromagnetic scattering of complex objects. *IEEE Trans Electromagnetic Compatibility* 24:397–405.
6. Li X, Taflove A, Backman V (2005) Modified FDTD near-to-far field transformation for improved backscattering calculation of strongly forward-scattering objects. *IEEE Antennas and Wireless Propagation Lett* 4:35–38.
7. Richards B, Wolf E (1959) Electromagnetic diffraction in optical systems. 2. Structure of the image field in an aplanatic system. *Proc R Soc London Ser A* 253:358–379.

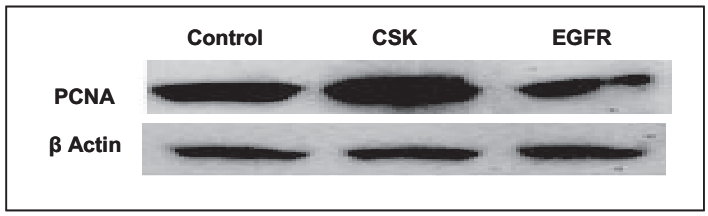

Fig. S1. Effect of knockdown of CSK and EGFR gene expression on cell proliferation: Knockdown of CSK and EGFR gene expression was achieved in human colon cancer cell line HT-29 by stable transfection of the CSK- and EGFR-specific shRNA vectors. HT-29 cells transfected with empty vector (control vector) was used as control. The cell lines were grown in McCoy's Modified 5A Medium (ATCC) at 37 °C in a humidified 5% CO_2 incubator. Total cellular proteins were extracted in 2× Lammeli Sample buffer. Equal amounts (40 μg) of protein samples were separated by polyacrylamide gel electrophoresis and transferred on PVDF membrane and probed with an antibody against the proliferation specific marker–proliferating cell nuclear antigen (PCNA) (Santa Cruz Biotechnology) overnight at 4 °C. Xerograms were developed with enhanced chemiluminescence (Santa Cruz Biotechnology). Images were acquired through UVP Bioimaging Systems (UVP) and analyzed by using Labworks 4.6 software (UVP). Consistency in protein loading was assessed by probing membranes with anti-β-actin (Sigma). Compared with the control vector, the CSK shRNA construct showed a 30% increase in the levels of PCNA ($P < 0.05$, indicating increased cell proliferation), whereas the EGFR shRNA construct showed a 27% decrease in PCNA ($P < 0.05$, indicating decrease in cell proliferation).

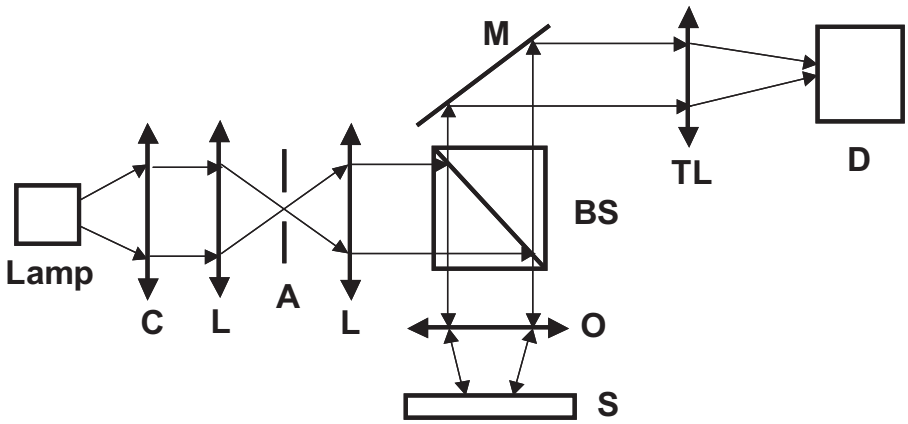

Fig. S2. Schematic of the partial-wave spectroscopy (PWS) system. (*A*) C,condenser; L, lens (f = 150 mm); A, aperture; BS, beam splitter; O, objective lens; TL, tube lens (f = 450 mm); S, sample; D, detector (including the imaging spectrograph (slit width = 10 μm, spectral resolution ≈3 nm; Acton Research) and CCD camera (CoolSnap HQ; Roper Scientific).

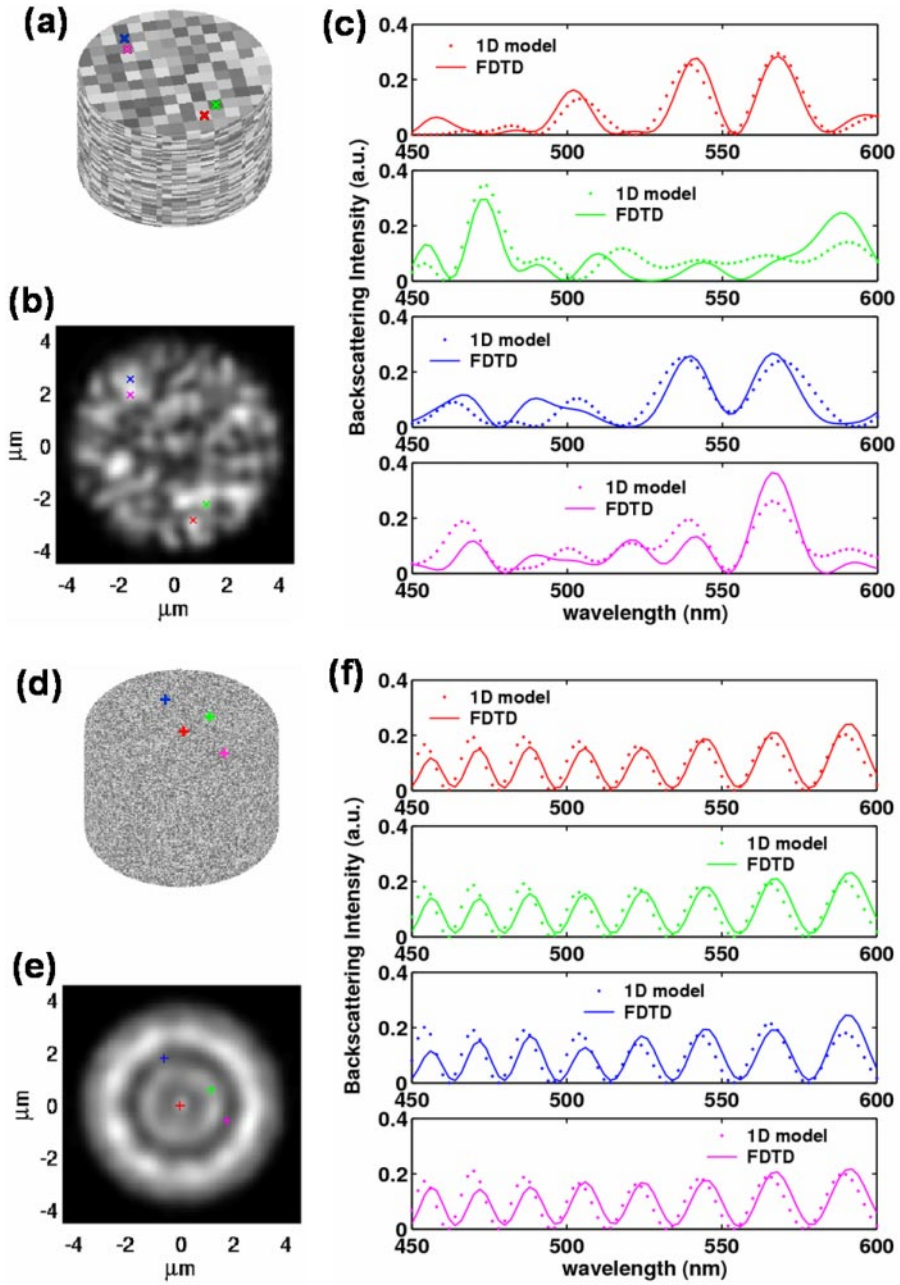

Fig. S3. FDTD simulations demonstrating the validity of using 1D model to analyze the back-scattered spectra of each pixel in the PWS image. (*A* and *D*) Geometry in the FDTD simulation. Here, an inhomogeneous dielectric cylinder with diameter of 8 μm and height of 5 μm is imported in the FDTD grid with 20-nm resolution. The cylinder has refractive index distributed randomly in 600 $\times$ 600 $\times$ 100-nm rectangular blocks (*A*) and in 60 $\times$ 60 $\times$ 60-nm rectangular blocks (*D*) with the mean refractive index $n_0 = 1.38$ and maximum refractive index fluctuation $\Delta n_{max} = 0.02$. In the FDTD simulation, the grid is terminated by using a Berenger perfectly matched layer (PML) absorbing boundary condition (4). The total-field/scattered-field (TF/SF) technique (5) is used to source an X-polarized plane wave propagating in the FDTD grid. We choose a modulated Gaussian pulse as the time-domain source waveform that accommodates the complete frequency range of visible light. The scattered-field frequency response is extracted via a discrete Fourier transform (DFT) of the time-domain data recorded on the 6 surfaces of the scattered-field region and normalized by the spectrum of the source pulse. A modified version of 3D near-to-far field transformation in the phasor domain (6) is implemented to calculate the far-field scattered wave in the backward direction. (b),(e) Synthesized back-scattering intensity image by applying the vector diffraction theory (7) to the far-field scattering fields calculated by FDTD. (*C*–*F*) Comparison of the FDTD-calculated back-scattering spectra at 4 locations in the synthesized microscope image (as shown by the color-coded markers in *B* and *E*) with that calculated by 1D slab model. The refractive index distribution in 1D slab model follows the point-spread function averaged vertical refractive-index distributions of pixels centered at the corresponding location in the FDTD geometry (displayed with color-coded markers in *A* and *D*).